Contents lists available at ScienceDirect

Chemical Engineering Journal

journal homepage: www.elsevier.com/locate/cej

Magnetic flexible sensor with tension and bending discriminating detection

Quan Shu [a], Zhenbang Xu [b], Shuai Liu [a], Jianpeng Wu [a], Huaxia Deng [a], Xinglong Gong [a,*], Shouhu Xuan [a,*]

[a] CAS Key Laboratory of Mechanical Behavior and Design of Materials, Department of Modern Mechanics, University of Science and Technology of China (USTC), Hefei 230027, China
[b] CAS Key Laboratory of On-orbit Manufacturing and Integration for Space Optics System, Changchun Institute of Optics, Fine Mechanics and Physics, Chinese Academy of Sciences, Jilin, Changchun 130033, China

ARTICLE INFO

ABSTRACT

The flexible wearable sensors with high sensitivity and stability provide wide potential in artificial intelligence and human–machine interaction. However, dual-modal sensor with contact and non-contact working mode based on a facile and cost-effective methodology which can recognize external stimulus forms remains a challenge. Especially, magnetic non-contact sensing performance has gained increasing attention in smart wearable device. This work reports a flexible and magnetic sensor based on a sandwich structure film (SSF) which can detect both tension and bending stimuli by supplementing opposite electric signal feedbacks. Notably, the $\Delta R/R_0$ of SSF sensor reaches 44.1% at 5% tensile strain and it presents excellent stability even after 10,000 cycles. Moreover, the $\Delta R/R_0$ of SSF sensor maintains at -17.2% under 2 mm bending displacement. Additionally, SSF sensor can be employed as electronic skin to perceive the human joint motion in real-time. Furthermore, the direction and density of magnetic field applied to SSF sensor can be clearly discriminated, thus a non-contact magnetic keyboard has been designed and developed. As a result, the facile manufacturing processes and outstanding multifunctional sensing characteristics endow SSF sensor with high implementation potential in the next-generation intelligent electronic equipment or systems.

1. Introduction

With the development of flexible electronic technology and artificial intelligence (AI), flexible sensors attract increasing attention in the next-generation application of human–machine interaction [1–8]. It is reported that dual-modal devices for both tactile sensing and non-contact perception is of great importance for the next generation of AI [9]. Moreover, contact mode based tactile sensors can directly detect the mechanical (e.g. pressure, strain, tensile, bend) or motional information from human body. Notably, flexible sensors incorporated with magnetic particles endowed the electronics with magnetic/stress coupling sensing capabilities [10], and magnetic actuating was beneficial for allowing the sensor to respond in non-contact manner [11–13]. Although the single working mode electronics toward magnetic field or strain sensing have been well developed, they still suffer from the monotonous detection of specific sources and thus are unable to satisfy the growing demand for multi-functions [14]. Hence, the dual-modal sensor with non-contact magnetic response and strain contact can not only respond to

mechanical stimuli *via* contact mode, but also the magnetic response non-contact interaction could be potentially applied to AI.

In comparison to the previous report [15], film sensors based on sandwich structure are attractive in smart electronics due to their simple fabrication and low cost characteristics [16–19]. During the past decade, most of the reported tactile sensors were sensitive to stretching or bending stimuli, showing a single mechanical response mode [20]. Wu et al. presented a composite film sensor which could sensitive to bending excitation and response with positive signals [20]. Interestingly, a flexible sensor that can monitor tension, compression and bending was proposed [21]. Nevertheless, the reported response of the sensor to tension, compression and bending were all feedbacks with positive signals, which was difficult to distinguish the form of mechanical stimulation by the relative resistance change of both positive signals [21]. More notably, flexible sensors for multi-modal perception with high stretchability and good flexibility (e.g. strain, bending) were attracted increasing attention [22,23]. However, flexible sensors that can respond to different mechanical stimuli with reverse signal

feedbacks are still scarce. Therefore, flexible tactile sensors with dual-modal working modes that can discriminate tension and bending excitation forms have become urgent demands for smart electronics.

The flexible sensors were usually applied in functional skin-like electronics [24], human glove [25], biomimetic acoustic band [26], and wearable touch keyboard application [27]. Liu et al reported a stretchable sensor with sandwich structure based on silver nanowires (AgNWs) conductive hybrid and polydimethylsiloxane (PDMS) matrix [28]. Due to the adjustability and controllability of magnetic particles, the magnetic film sensors exhibited a typical non-contact sensing behavior [9]. However, the lack of the designation confines the application of the non-contact magnetic film sensors with sandwich structure. Moreover, various equipment and systems, such as keyboard systems [27], home appliance remote control, and public elevators always required frequent human touch [2]. Because of the inevitable mechanical wear and fatigue limitations [29], conventional contact sensing and operation are difficult to avoid these deficiencies. In addition, direct contact of living facilities in environments with poor medical conditions may infect potential bacteria or viruses. In this case, non-contact flexible sensors with ultra-stability which can protect people away from the spread of bacteria and viruses have attracted a growing attention in the next-generation of AI [30–33]. As a result, a magnetic non-contact control system is urgently required.

Herein, a multi-modal sandwich structure film (SSF) sensor composed of h-MRE-AgNWs-PDMS (h-MRE, NdFeB/PDMS hard magnetic magnetorheological elastomer) was fabricated by a simple and cost-effective method. The tension and bending mechanical stimuli of the SSF sensor could be discriminated by presenting the contrary electric signal responses. Moreover, a magnetic electronic skin based on the SSF sensor was developed for human movement monitoring. Due to the inherent hard magnetic characteristic of NdFeB, the SSF sensor exhibited significant electric signal changes under applying different magnetic field densities and directions. At last, a non-contact smart keyboard was fabricated based on the magnetic sandwich structure, in which digital signals could be converted and transmitted in a wireless Bluetooth mode.

2. Experimental section

Materials: The PDMS (type Sylgard 184) precursor and curing agent were purchased from Dow Corning GmbH, USA. NdFeB particles were supplied from Guangzhou Nuode Transmission Parts Co., Ltd, China. The average size of NdFeB particles is 5 μm. The raw materials for self-prepared silver nanowires (AgNWs) solution [34] contained Polyvinylpyrrolidone (PVP), $AgNO_3$, glycerol, ethanol and NaCl were from Sinopharm Chemical Reagent Co., Ltd.

Fabrication of sandwich structure sensor: The U-shaped pattern was designed and optimized in CAD software. A commercial polyethylene terephthalate film (thickness: 14 μm) was hollowed out into the designed pattern *via* the laser cutting technology. The reusable masking films were obtained. Here, the designed U-shaped pattern was used to prepare the sensor with good response and flexibility.

h-MRE precursor (PDMS curing ratio of 20:1, NdFeB particles mass fraction of 50 wt%) was prepared by stirring the mixture for 5 min, and then vacuum treated for 10 min to remove the bubbles. The h-MRE precursor was poured onto a silicon (Si) wafer, spin-coated at 500 rpm for 15 s and 1000 rpm for 20 s, then cured at 90 °C for 3 min. After curing, the masking film was attached to the cured h-MRE film. The paths of pattern were coated with solution of AgNWs (concentration: 8.7 mg/mL) and dried at 35 °C plate for 5 min. This coating operation was repeated for 5 times to form conductive AgNWs network, and then the h-MRE@AgNWs was cured at 90 °C for 10 min. After the h-MRE@AgNWs was formed, the masking film was peeled off. The wires were adhered to the electrode zones of conductive pattern by silver paste. After that, the pre-PDMS mixture was poured on the surface by spin coating at 500 rpm for 15 s and 1000 rpm for 20 s to completely

cover the pattern, and cured at 90 °C for another 10 min. Here, the sandwich structure film (SSF, including h-MRE@AgNWs@PDMS) sensor was formed. The SSF sensor was released from the silicon wafer by manual peeling (Fig. 1a (i)). In addition, the pre-h-MRE mixture was poured on the surface of h-MRE@AgNWs by spin coating at 500 rpm for 15 s and 1000 rpm for 20 s, and the h-MRE@AgNWs@h-MRE sensor was formed after curing at 90 °C for 10 min.

Characterization: The microstructures of the h-MRE@AgNWs and SSF were observed by scanning electron microscope (SEM, Philips of Holland, model XL30 ESEM-TMP) under 3 kV. The hysteresis loops of isotropic h-MRE, h-MRE@AgNWs and SSF were tested by Hysteresis Measurement of Soft and Hard Magnetic Materials (HyMDC Metis, Leuven, Belgium). The tensile and bending test system consists of a dynamic mechanical analyzer (DMA, ElectroForce 3200, TA instruments, Minnesota 55,344 USA) and Modulab MTS (Solartron analytical, AMETEK advanced measurement technology, Inc., United Kingdom). The magnetically response tests were finished by Modulab MTS with a DC power electromagnetic coil.

3. Results and discussion

3.1. Preparation and characterization of h-MRE@AgNWs and SSF

Fig. 1a (i) depicts the schematic preparation process of sandwich structure sensor and the fabrication steps were mainly manifested in the low materials dosage and simple preparation. The procedure mainly involved four steps: (i) spin-coating and vulcanizing of pre-h-MRE mixture (20:1 curing ratio) on a silicon wafer, (ii) dip-coating of AgNWs solution by the employment of a reusable masking film, (iii) completing the curing, peeling of masking film and the attachment of conductive electrode, (iv) spin-coating and curing of pre-PDMS matrix. Finally, the cured sandwich-structured film was peeled from the silicon wafer and the flexible sensor was created. As shown in Fig. S1a, the cross-sectional SEM image of SSF sensor presents a typical sandwich structure. Here, magnetic matrix and AgNWs film endow the sensor with excellent magnetoelectric performance. Therefore, SSF sensors possess great potential in flexible electronic skin and non-contact signal transmission (Fig. 1a (ii)). Fig. 1b is the optical image of h-MRE@AgNWs product, which demonstrates the length of U-shaped pattern conductive path is 50 mm and the width of the path is 3 mm. After peeling off, the flexible SSF sensor is obtained (Fig. 1c). Owing to the spin-coating process, the thickness of sandwich structure is very thin and it can be controlled to 310 μm (Fig. S1b). The SSF sensor exhibits a good flexibility and it can be deformed by tensile and bending (Fig. 1d and 1e). As a result, the SSF sensor is controllably fabricated by a facile method, and the sensor exhibits excellent elasticity and deformability.

The detailed inner nanostructure of the sandwich structure film sensor are displayed in Fig. 2. SEM image presents the h-MRE@AgNWs film has a U-shaped pattern structure and the SSF sensor has a simple and typical conductive path (Fig. 2a). Obviously, the AgNWs are aggregated together to form the uniform layer and they are reticulately assembled in the U-shaped pattern (Fig. 2b, c). Thus, the SSF sensor has a stable resistance. Fig. 2d and Fig. S1a present the SEM images of the macro-scale sandwich structure (PDMS-AgNWs-h-MRE) and micro-cross section of the SSF sensor, respectively. Obviously, the thickness of AgNWs layer is about 14.21 μm (Fig. 2d) and this conductive layer is tightly combined by both of PDMS and h-MRE, therefore the AgNWs are well sandwiched between the two matrix (Fig. 2e). Moreover, in the isotropic h-MRE layer, the NdFeB particles are randomly distributed in the matrix (Fig. 2f). Due to the wonderful hard magnetic NdFeB, the SSF sensor exhibits good magnetic property.

Fig. 2g shows the tension mechanical properties of the SSF, which demonstrates the tensile fracture force and fracture displacement of SSF sensor is 1.5 N and 38.45 mm, respectively. Here, the lower breaking force and the higher tensile displacement length indicate that the SSF sensor has good elasticity and flexibility. Originated from the NdFeB
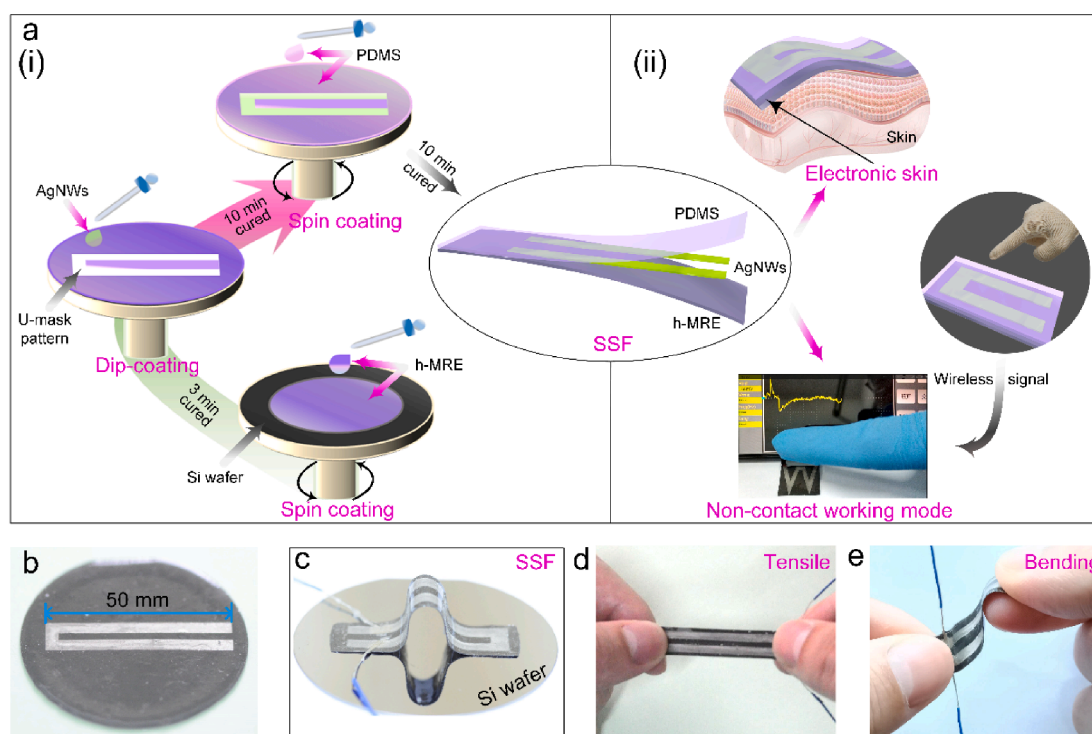
Fig. 1. (a) Preparation process of SSF (i) and the potential application of SSF sensor in electronic skin, the wireless signal operation and non-contact working mode (ii); (b) the optical images of h-MRE@AgNWs, and (c) SSF sensor under (d) tensile and (e) bending stimuli.

particles, SSF sensor presents a typical hard magnetization. The saturation magnetizations of h-MRE, h-MRE@AgNWs and SSF are 65.2 emu/g, 52.0 emu/g and 38.6 emu/g, respectively (Fig. 2h). Due to the presence of the conductive AgNWs layer, the SSF sensor presents a good electrical property. Here, the effect of dip-coating cycles on electrical performances of SSF sensor was also investigated. As shown in Fig. 2i, with increasing of the dip-coating cycles, the mass content of AgNWs increases, thus its resistance decreases.

3.2. Mechanic electric coupling behavior of the SSF sensor

The mechanical excitation responsive performances of SSF sensor were systematically investigated by using an Electroforce system and an electrical property test system Modulab MTS. The influences of the tensile strain, signal waveforms, loading frequencies and its response time, sensitivity, and cycle stability were measured and evaluated. Fig. 3a exhibits the image of SSF sensor under tensile stimulus. It is obvious that the conductive path produces significant radial tensile deformation under external load excitation. Therefore, the sharp increment of the resistance must be responded for the radial deformation of the AgNWs layer. As shown in Fig. 3b and c, SEM images show the microstructure changes of AgNWs network under tension. Clearly, significant cracks appear in the AgNWs network compared to the initial state. Therefore, the conductive path of the SSF sensor is damaged under tension. Fig. S2a presents the relative resistance change ($\Delta R/R_0$) of SSF sensor at a low tensile strain of 0.25%–1.25%, where R_0 is the initial electrical resistance and ΔR is the resistance variation. The inset in Fig. S2a is an enlarged view of 1% strain, which demonstrates the response of the SSF sensor is stable. Due to the good flexibility, the applied tensile strain can vary from 0.25% to as high as 37.5%, and the $\Delta R/R_0$ of SSF sensor increase from 0.95% to 1079.1% (Fig. 3d). Obviously, $\Delta R/R_0$ increases with increasing of the tensile strain. By keeping the frequency at 0.5 Hz, the cyclic loading is conducted for 10 cycles, and the $\Delta R/R_0$ almost keep at a constant value (Fig. 3e). Here, the SSF sensor maintains a good stability and conductivity throughout the tensile deformation stage.

When the frequencies were varied from 0.01 Hz to 1 Hz, the electrical results of SSF sensor were similar (Fig. 3f). Therefore, the loading frequency showed few influence on the sensing behavior of SSF sensor. In addition, the tensile strain was set at 5% to investigate its sensing relationship with different loading waveform, such as sine wave, triangular wave, and square wave (Fig. 3g). The electrical signal responses of SSF sensor were consistent with the tensile strain time curves. Furthermore, by keeping 0.5 Hz frequency and 5% tensile strain, the loading of SSF sensor were evaluated for 10,000 cycles. As shown in Fig. 3h, it can be concluded that the SSF sensor shows a good durability and robustness.

Finally, the sensing ability of the SSF sensor was analyzed by investigating the tensile strain dependent $\Delta R/R_0$ with strain varied from 0.25% to 37.5% (Fig. 3i). The sensitivity coefficients are approximated to three response ranges with the corresponding tensile strain divided into 0.25% to 5%, 7.5% to 30%, and 32.5% to 37.5%, respectively. The insets of Fig. 3i represent enlarged view of the 0.25% to 5% (the first range) and 32.5% to 37.5% (the third range), respectively. Additionally, the slope embedded in Fig. 3i represents the gauge factor (GF, $(\Delta R/R_0)/\Delta\varepsilon$) of the first range and the third range. Within the first range, the GF is 9.09. As the tensile strain increased from 32.5% to 37.5% (the third range), the $\Delta R/R_0$ increased from 732.2% to 1079.1%. In the third range, the GF of SSF sensor is calculated to be 66.66, which must be responded for the high resistance change in the large tensile strain range. As a result, the SSF sensor exhibits excellent stability and superb sensitivity during the tension process.

Due to the Mullins effect, the rubbery substrate and sealing layer was strain softened, so after tension for many cycles, the response of SSF sensor attenuated. As shown in Fig. 4, the SEM images depicts the microstructure changes of AgNWs after tensile loading–unloading. The SEM images of the AgNWs layer after 200 cycles and 10,000 cycles are shown in Fig. 4a and d, respectively. Clearly, the number of cracks in Fig. 4d is significantly greater than that in Fig. 4a, i.e., where the increase in the number of tensile loading–unloading cycles is proportional
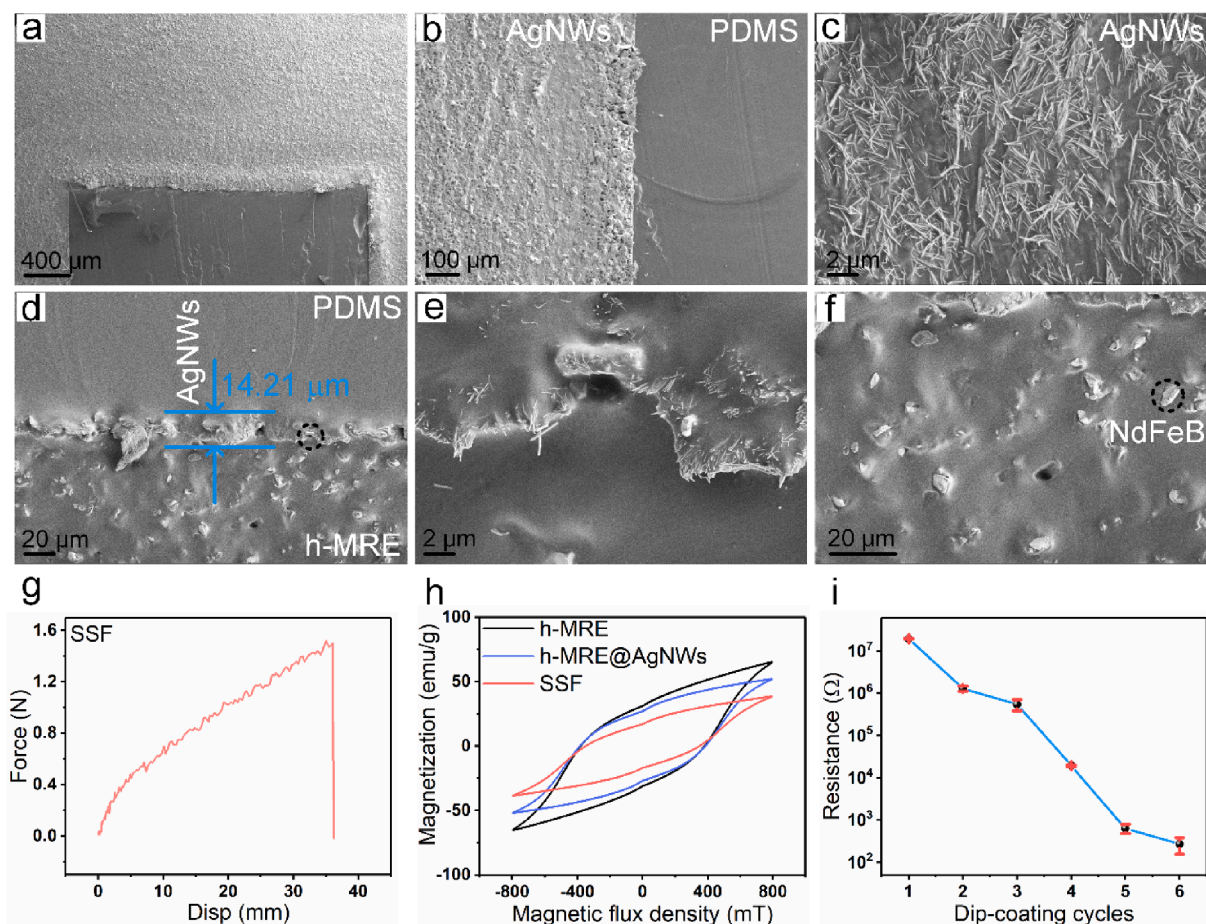
Fig. 2. SEM images of (a) h-MRE@AgNWs and (b) border of the U-shaped pattern; (c) Magnified image of the AgNWs conductive network; SEM images of cross section: (d) SSF and (e) the enlarged area of AgNWs layer; (f) SEM image of NdFeB particles in the h-MRE matrix; (g) Tensile fracture performance of SSF; (h) Saturation magnetization of h-MRE, h-MRE@AgNWs and SSF; (i) Resistance of SSF sensor with different dip-coating cycles.

to the increased number of cracks. After 200 tension cycles, the AgNWs remains connected to each other among the cracks, which ensures the stable electrical properties of the conductive layer (Fig. 4b and c). Similarly, the AgNWs still maintain the connection between the cracks after 10,000 tension cycles, which demonstrates the good stability and excellent electrical performance of the SSF sensor in repeated cycles (Fig. 4e and f). Here, in order to illustrate the universality of SSF sensor, the third range strain was selected for the tensile loading–unloading cycles. The durability and robustness of SSF sensor was evaluated for 10,000 cycles at 32.5% tensile strain (Fig. 4g). The $\Delta R/R_0$ of SSF sensor was about 739.8 % after 1350 cycles. After 5000 cycles of loading–unloading under tension, the $\Delta R/R_0$ of SSF sensor remained at 743.5%. Moreover, the $\Delta R/R_0$ of SSF sensor was maintained at 744.7% during 8450–8464 tension cycles, which indicated the good repeatability and high stability of the SSF sensor.

Fig. 5a shows the optical image of SSF sensor under bending excitation. Clearly, the conductive path was obviously bent and deformed under external curling stimuli. As shown in Fig. 5b and c, SEM images present the microstructure of AgNWs network after bending. Obviously, in comparison to the pristine state, the AgNWs network is stacked more densely. As the bending displacement increases, the $\Delta R/R_0$ of SSF sensor gradually decreases (Fig. 5d). Interestingly, different from the tensile loading, the resistance of the sensor decreases with the bending loading. Particularly, the $\Delta R/R_0$ decreases from −0.39% to −18.1% when the bending displacement increases from 0.1 mm to 5 mm. The electrical response behavior of the SSF sensor under loading and unloading stimulus was investigated (Fig. 5e). The results show that SSF sensor

exhibits good resilience characteristics, which provides a good choice for the practical application of the film sensor. As a result, the different change behavior of the resistance is favorable for distinguishing the loading mode.

As shown in Fig. 5f, the electrical signal feedback of SSF sensor is consistent with the details of bending displacement time curves under 2 mm bending displacement. It demonstrates that different loading waveforms of bending can be well responded by the SSF sensor. Additionally, the frequency of bending stimuli hardly influence the sensing behavior of SSF sensor when the frequencies increases from 0.01 Hz to 1 Hz (Fig. 5g). Similar to the tension loading, the frequency presents few influence on the perception performance of the SSF sensor in the bending. Moreover, the durability and robustness of SSF sensor was evaluated for 10,000 cycles at 0.5 Hz frequency and 2 mm bending displacement (Fig. 5h), exhibiting the high stability and good repeatability. The initial resistance of the SSF sensor was about 114.4 Ω. After 4000 cycles of loading and unloading under bending, the initial resistance almost remained constant. Moreover, after 10,000 cycles, the initial resistance changed to 111.7 Ω, which indicated the high stability of the SSF sensor. Similarly, the rubbery substrate and sealing layer was strain softened due to the Mullins effect, so the response of SSF sensor attenuated after cycling bending. After several hundred bending cycles, the rubbery matrix gradually adapts to the strain softening effect and the electrical response of SSF sensor remains stable.

Fig. 5i shows the relationship of $\Delta R/R_0$ and bending displacement. The sensitivity coefficients are approximated to the two response ranges, and the corresponding bending displacement are 0.1 mm to 1.5 mm (the
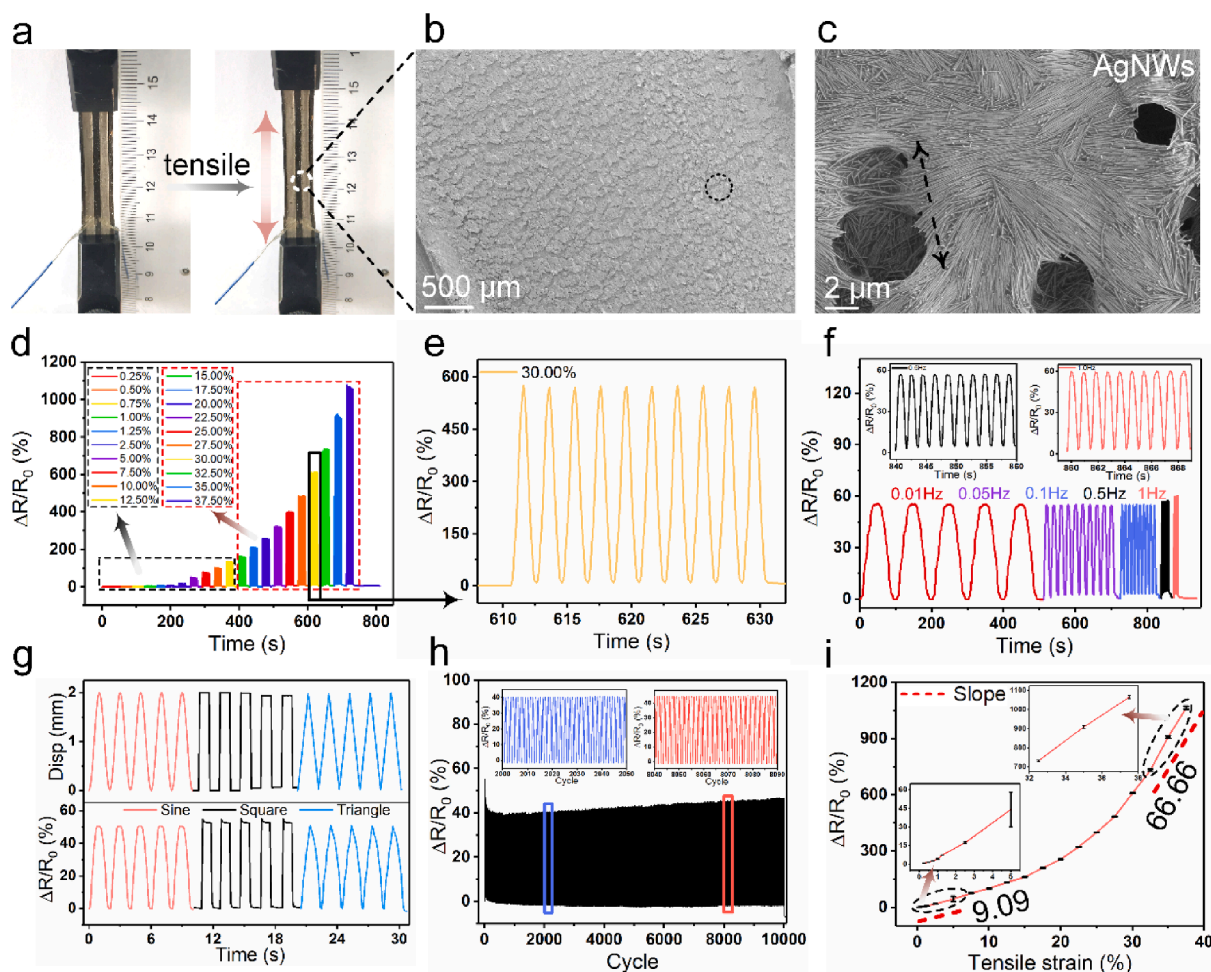
Fig. 3. (a) The image of SSF sensor under tensile loading; SEM images of (b) AgNWs layer and (c) magnified view of AgNWs under tensile excitation; (d) Variation of the $\Delta R/R_0$ under tensile strain increased from 0.25% to 37.5% at frequency of 0.5 Hz; (e) Magnified curve of $\Delta R/R_0$ under the tensile strain of 30 %; (f) Real-time monitoring of $\Delta R/R_0$ with different frequencies; (g) Displacement change for different waveforms and the corresponding electrical performance at a frequency of 0.5 Hz; (h) Real-time monitoring of the resistance variation in the cyclic loading and unloading of tensile strain; (i) Relative electric resistance change *vs* tensile strain. Inset: the enlarged area of $\Delta R/R_0$ *vs* tensile strain ($\Delta \varepsilon$).

first range) and 2 mm to 5 mm (the second range), respectively. The embedded image in Fig. 5i represents magnified image of the first range. Here, the GF is defined as $(\Delta R/R_0)/\Delta l$, where the Δl represents relative bending displacement change. The GF of the first range and second range is -11.2% mm^{-1} and -0.3% mm^{-1}, respectively. It is clear that SSF sensor possess high sensitivity in the first range. However, with increasing of the bending displacement, the sensitivity gradually decreases. Therefore, this method provides an option for the actual application of sensors within the low bending range. Based on the above analysis, it is concluded that the tension and bending stimuli can be clearly discriminated by the SSF sensor with positive and negative electrical responses.

Here, the sensing mechanism of SSF sensor in response to tensile and bending stimulation was explored. Fig. 6a presents the schematic diagram of U-shaped AgNWs layer under normal state without loading excitation. The AgNWs are uniformly distributed in the conductive layer, which are also tightly embedded within the PDMS matrix. Due to the Poisson effect, U-shaped conductive layer produced radial deformation when SSF sensor was subjected to radial tensile loading, resulting in the damage of conductive path (Fig. 6b). The AgNWs network was radially fractured under tensile traction and the number of contact nodes between the AgNWs decreased. Therefore, the conductive path was destructed, which led to an increase in sensor resistance. As shown in Fig. 6d, many cracks are found in the AgNWs network, which must

destroy the conductive microstructure and increase the resistance.

Fig. 6c presents the schematic diagram of conductive layer structure under bending. When the U-shaped conductive layer was subjected to bending stimulus, the contact nodes number between the AgNWs increased due to the squeezed deformation. In this case, the connections between the AgNWs conductive network became much tighter. Therefore, the resistance of SSF sensor decreased under bending load. The SEM image shows the surface structural of the AgNWs layer changes during the bending and extrusion (Fig. 6e). As a result, the final SSF sensor can be used to detect the mode of the external stimuli. Fig. 6f shows the electrical behavior response of SSF sensor under the excitations of tensile and bending. Clearly, SSF sensor can notably distinguish the difference between tensile and bending stimuli. The SSF sensor presented a positive signal when loaded by tension and exhibited a negative signal response when motivated by bending excitation.

3.3. Human perception performance of the SSF sensor

Owing to the wonderful mechanic-electric coupling behavior, the SSF sensor possess high potential in physiological signal sensing and control command transmitting. Here, the sensing performance of the SSF sensor on detecting joint motion was investigated. Fig. 7a depicts the schematic diagram of the test device and principle. The SSF sensor was connected with the Modulab materials test system (MTS) to form a loop,
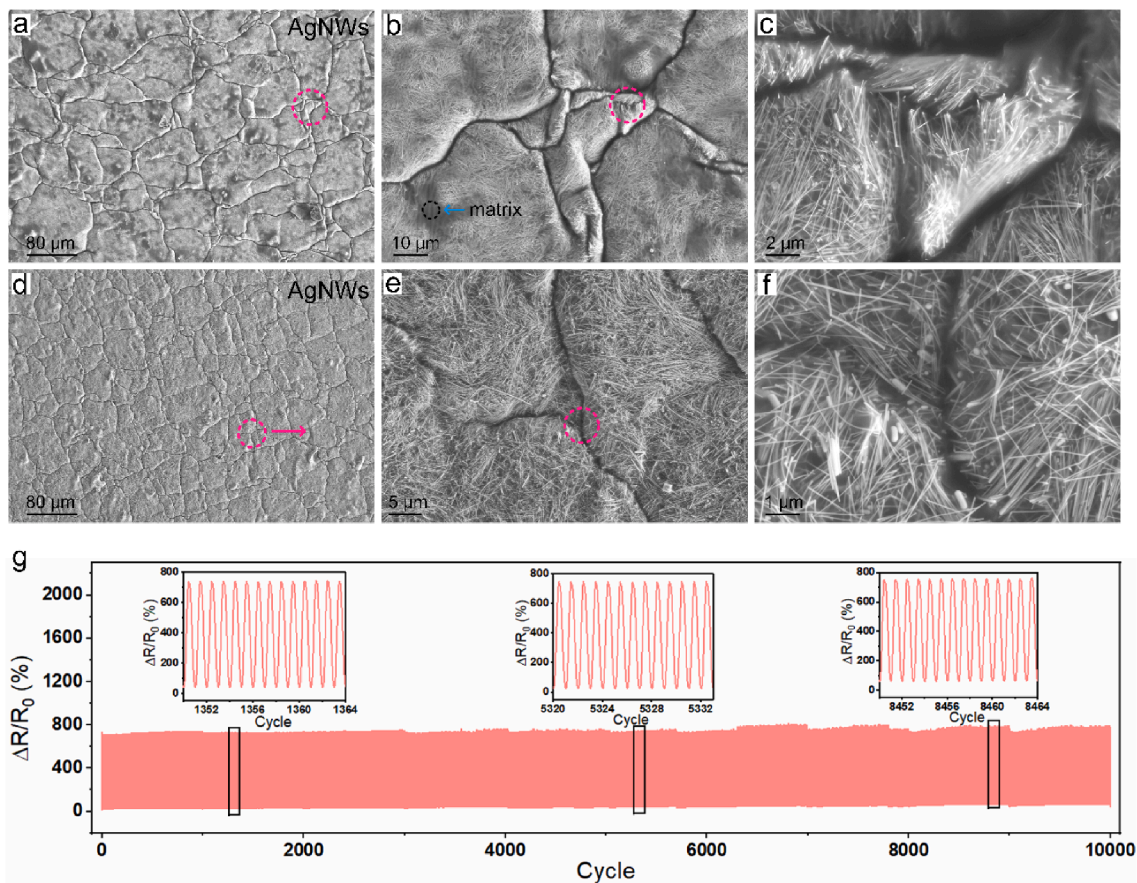
Fig. 4. SEM images of (a) AgNWs layer after 200 tension loading–unloading cycles, (b) magnified view of AgNWs, and (c) the enlarged area of the cracks between the AgNWs; SEM images of (d) AgNWs after 10,000 tension loading–unloading cycles, (e) magnified view of AgNWs, and (f) the enlarged area of the cracks between the AgNWs; (g) The $\Delta R/R_0$ of SSF sensor in 10,000 loading–unloading cycles at 32.5% tensile starin.

and the MTS was connected with the pre-programed control system to display the real-time resistance changes. Here, the sandwich structure sensor can monitor the human joint activity by outputting electric signals to perceive the action behavior of actual human life. Fig. 7b presents the real-time response to the joint motion when the SSF sensor was attached to the finger. Obviously, the electrical signals response gradually increases with increasing of the finger motion range. As shown in Fig. 7c is the electrical signals response on the bending angle of the wrist. Clearly, the $\Delta R/R_0$ increases from 6.9% to 9.9% once the angle decreases from 122° to 92°. Moreover, when the angle of elbow bending increases from 26° to 120°, the $\Delta R/R_0$ of SSF sensor varies from 17.7% to 78.5%, respectively (Fig. 7d).

Here, the SSF sensor was tightly attached to the skin surface. When the wrist gradually bent inward, the sensor suffered from the tensile traction. Therefore, the contact nodes of AgNWs conductive network decreased, which led to the increment of the resistance. Furthermore, the electrical response of the SSF sensor to continuous repeated joint motion was tested. As shown in Fig. 7e, the knee was repeatedly bent for 8 times and in real-time monitoring demonstrated the detection was stable. Moreover, the SSF sensor also performed well in the perception of drinking water (Fig. 7f). In this case, drinking water four consecutive times, the $\Delta R/R_0$ almost remained constant 6.2%. Undoubtedly, the SSF sensor shows excellent stability, responsiveness and sensitivity for real-time monitoring continuous joint movement.

3.4. Magnetic electric coupling behavior of the SSF sensor

Because the SSF matrix possess hard magnetic particles, the SSF

sensor also can be employed as a magnetic actuator with self-sensing ability. Here, the actuating behaviors of the SSF sensor under various external magnetic field were explored. To further evaluate the influence of NdFeB particles, both the SSF and h-MRE@AgNWs@h-MRE sensor were fabricated and their response to the magnetic field with different directions were analyzed. The applied direction and magnitude of the magnetic field induced by controllable electromagnet can be controlled during the sensing. The electric response to magnetic field perpendicular to the conductive path was investigated. Firstly, the electromagnet was placed and a 3D printed mold was fixed on the surface of the magnet to carry the SSF sensor. The magnetic flux density was applied on the sensor by controlling the magnitude of the current applied to the electromagnet. Fig. 8a illustrates the schematic procedure of magnetic-electric performance testing. The NdFeB particles embedded in the SSF are hard magnetic, thus the SSF sensor shows a typical anisotropic magnetic behavior. As a result, by varying the direction of the external magnetic field, the SSF sensor receives attractive or repulsive force, respectively (Fig. 8b and c).

The real-time sensing properties of SSF sensor to different magnetic flux densities and magnetic field directions were demonstrated in Fig. 8d, e. As shown in Fig. 8d, the $\Delta R/R_0$ of SSF sensor increases from 1.9% to 9.9%.When a positive magnetic field was applied to the sensor, the SSF sensor was attracted to the magnet. With increasing of the magnetic field density from 45 mT to 205 mT, the tensile deformation of the SSF sensor become more significant due to the magnetic field attraction (Fig. 8h). Therefore, the positive electrical signal response of SSF sensor gradually increases obviously with the magnetic field (Fig. 8d). Furthermore, when the direction of the magnetic field was
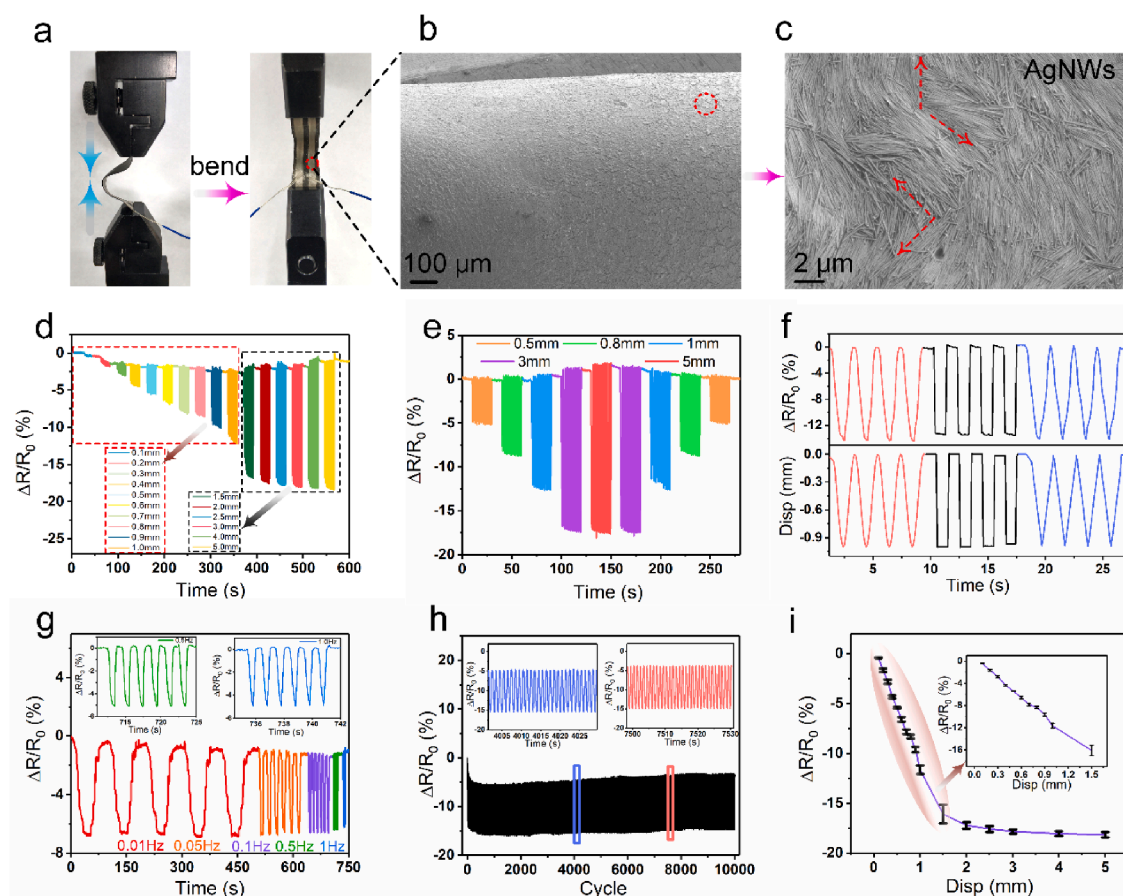
Fig. 5. (a) Optical image of SSF sensor under bending excitation; SEM images of (b) AgNWs layer and (c) AgNWs under bending; (d) Bending sensing performance with different bending displacement at frequency of 0.5 Hz; (e) The $\Delta R/R_0$ of SSF sensor under loading and unloading process; (f) Displacement change for different waveforms and the corresponding electrical performance at a frequency of 0.5 Hz; (g) Real-time $\Delta R/R_0$ response with different frequencies; (h) The stability under 10,000 cycles bending; (i) $\Delta R/R_0$ *vs* bending displacement. Inset: the enlarged area of bending displacement increased from 0.1 mm to 1.5 mm.

changed, SSF sensor exhibited repel force, which was originated from the magnetic field-NdFeB interaction. As the magnetic flux density increases from 45 mT to 205 mT, the repulsion phenomenon increases significantly (Fig. 8g). Here, when the SSF sensor exhibited repulsion phenomenon in the reverse magnetic field, the conductive path was also stretched and deformed. Fig. 8e depicts the magnetic repulsive force of SSF sensor under the reversed magnetic field, which increases the $\Delta R/R_0$ of the sensor from 0.7% to 2.9%. The inset images of Fig. 8d and e show the deformation of SSF sensor under the reverse magnetic fields. Compared to repulsive force, the SSF sensor is more sensitive to magnetic attraction (Fig. 8f). Moreover, with increasing of the magnetic flux density, the sensitivity gradually decreased. Therefore, the magnetic sensor is suitable for low-magnetic field monitoring.

Owing to the repulsive force, curling deformation was obviously occurred on both sides of the SSF sensor, and the inner AgNWs layer generated a weak tensile deformation. Conversely, the conductive path of SSF sensor produced significant tensile deformation under the attractive force, so the $\Delta R/R_0$ changed more remarkable. Fig. S4a–c depict the $\Delta R/R_0$ of h-MRE@AgNWs@h-MRE sensor under different magnetic fields. The h-MRE@AgNWs@h-MRE sensor exhibits similar electrical response performance under attractive and repulsive stimuli. The sandwich structure h-MRE@AgNWs@h-MRE sensor has two layers of h-MRE films, while SSF sensor possess one h-MRE layer and one PDMS layer. Since the top and bottom layers of h-MRE@AgNWs@h-MRE sensor have the same structure, the $\Delta R/R_0$ under the varied magnetic field shows a small difference. The deformation process of h-MRE@AgNWs@h-MRE sensor under different magnetic fields is

recorded in Fig. S4d and S4e. Many complicated deformation is observed in the high magnetic field area. Therefore, the h-MRE@AgNWs@h-MRE sensor is more suitable for detecting the weak magnetic field due to the complex magnetic dipole–dipole interaction of the NdFeB particles in the matrix.

3.5. Non-contact sensing of the SSF

During the past decade, various diseases were generated from the fingers by carrying germs into the mouth. Recently, COVID-19 has swept the world, killing many people and healthcare workers. Many efforts have been made to fight the COVID-19. Herein, to reduce the occurrence of contact infectious diseases, a non-contact magnetic control keyboard was proposed. People frequently touch and use a computer keyboard in daily work, and without washing hand in time, a large number of bacteria still remain on fingers (Fig. 9a, (i)). Furthermore, for people with poor resistibility and insufficient health conditions, the probability of disease generation and spread is greatly increased. Therefore, a non-contact magnetic control keyboard based on wireless Bluetooth transmission signal acquisition system is designed and developed (Fig. 9a, (ii)).

Fig. 9b shows the image of non-contact magnetic keyboard, designed with a complete alphabet for simplicity. Fig. 9c shows the wireless non-contact keyboard sensing system and Fig. 9d depicts the circuit of the sensing system. Firstly, the external power supply connected the non-contact keyboard to generate a conductive loop, and the wireless Bluetooth transmission system was connected to the keyboard to collect
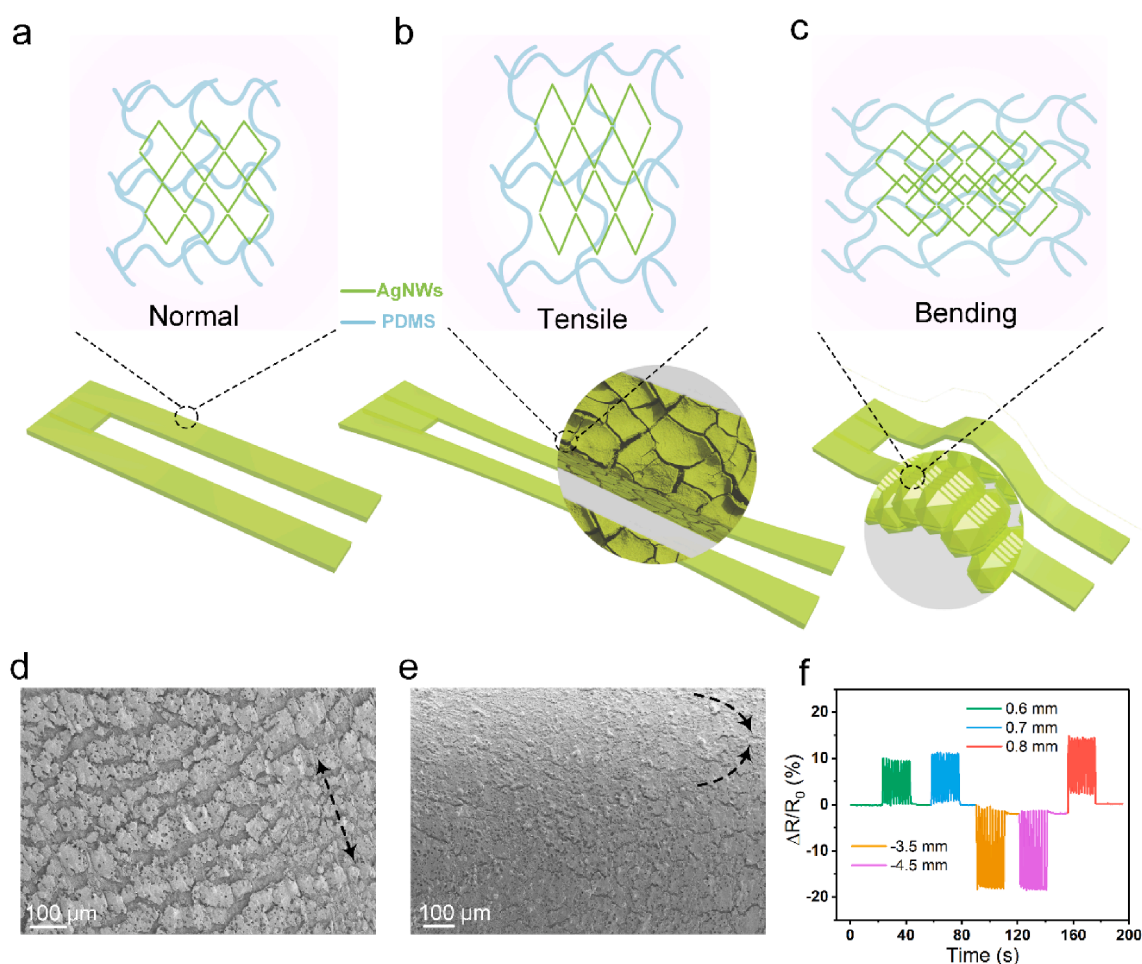
Fig. 6. Schematic diagram of U-shaped conductive layer and inner AgNWs network under different status: (a) normal state without tension and bending, (b) tensile and (c) bending stimulation; SEM images of AgNWs layer under (d) tension and (e) bending; (f) Electrical performance of SSF sensor under tensile and bending stimulation.
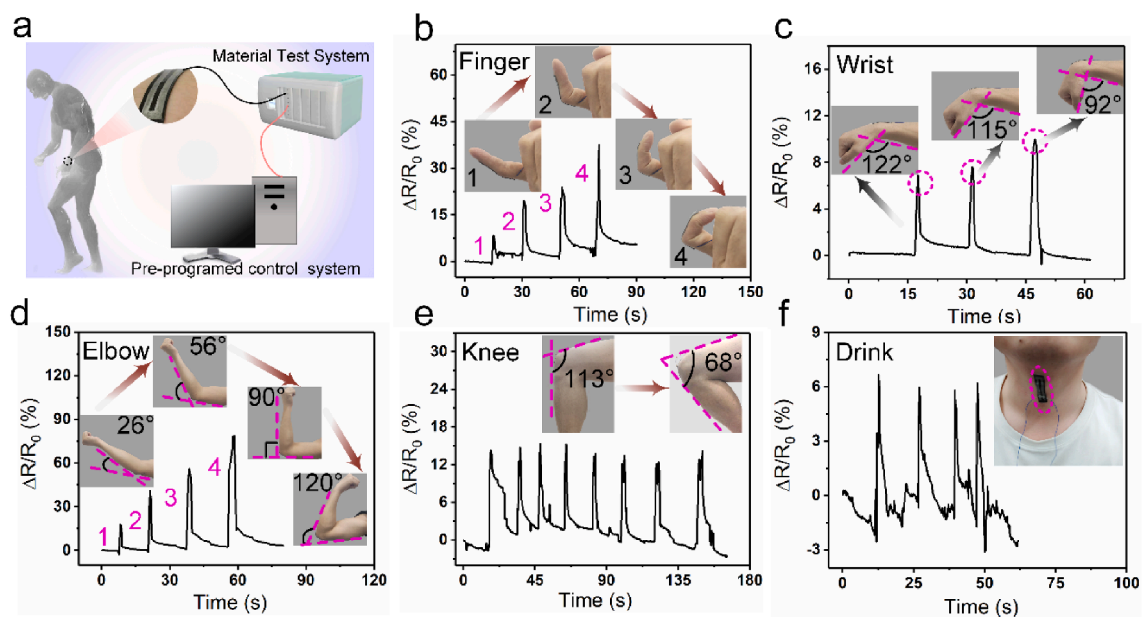

Fig. 7. Human body perception test. (a) Schematic diagram of test device and principle; Monitoring of (b) finger, (c) wrist, (d) elbow, (e) knee, and (f) drinking water.
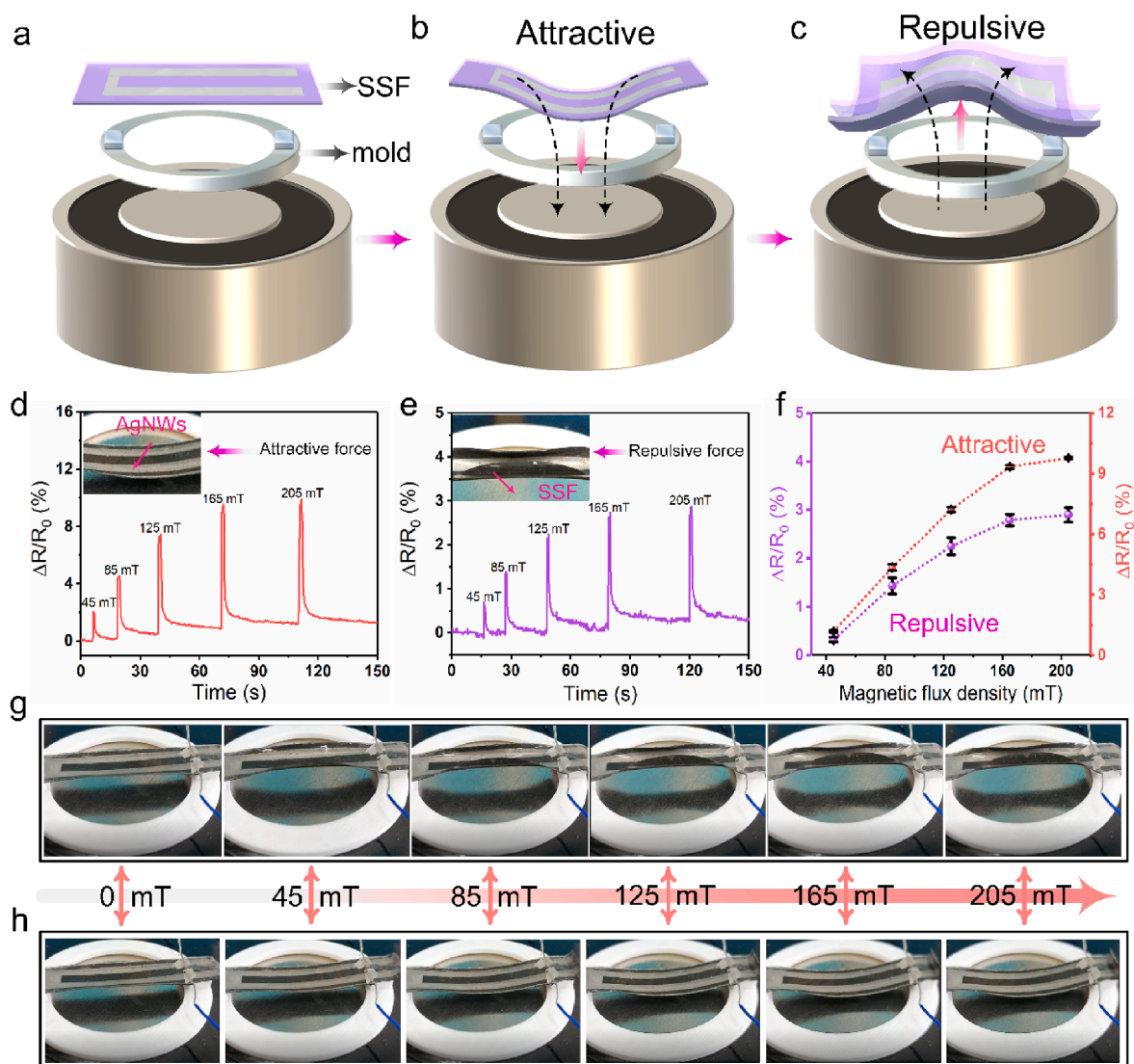
Fig. 8. The schematic diagram of (a) magnetic response test, under (b) attractive force and (c) repulsive force; The $\Delta R/R_0$ of SSF sensor under different magnetic field directions with (d) attractive force and (e) repulsive force; (f) The $\Delta R/R_0$ of SSF under attractive and repulsive force *vs* magnetic flux density; The optical images of SSF sensor under different magnetic response: (g) repulsion and (h) attraction.

resistance signals. Then, by the Bluetooth transmission system, the resistance signals were converted into voltage signals and transmitted to the mobile phone client, and the voltage signals change were displayed by client software. Finally, the real-time electrical signal feedback on the client software was obtained. Before preparing a complete keyboard, a single alphabet was first fabricated, and its size could be adjusted. Fig. S7a–c presents the electrical signal response generated *via* Bluetooth transmission of a single alphabet inspired by non-contact of magnetic gloves. To further investigate the relative resistance changes of single alphabet under the stimulation of magnetic gloves, the same non-contact test by using Modulab MTS was performed. Fig. 9e–f and Fig. S8 show the images of the non-contact electricity test of the single alphabet and the corresponding resistance change (Movie S1). After performing non-contact signal response test on single alphabet and obtaining valid feedback result, the same test on the magnetic control keyboard was conducted. Fig. S7d shows the image of non-contact sensing test and real-time signal feedback on client software. Similarly, Fig. 9g–h present images of the non-contact magnetic-electric test of the keyboard (Movie S2). Since the glove and the magnetic keyboard contained a permanent magnet and NdFeB particles, respectively, they

were gradually attracted when they got close. Therefore, the keyboard was deformed under the stimulation of the magnetic field, which caused the electrical signal of single alphabet to change. The resistance of the magnetic keyboard changed from 269.7 Ω to 524.6 Ω after first excitation of the magnetic gloves. Finally, the magnetic keyboard can be easily constructed by using the SSF sensor.

4. Conclusions

In summary, a sandwich structure film sensor with excellent flexibility, ultrahigh response time, and outstanding stability properties was developed by using mask-patterning and spin-coating technology. The U-shaped pattern conductive layer enabled the stretching and bending stimuli to be discriminated by the SSF sensor *via* outputting clear positive and negative electric signal, respectively. For instance, the $\Delta R/R_0$ of SSF sensor reached to 1064.5% and −18.2% when the tensile strain was 37.5% and bending displacement was 5 mm, respectively. In addition, SSF sensor can be used as electronic skin to sensitively perceive human joint motion. Moreover, the applied orientation and strength of magnetic field can be readily perceptible. When the magnetic flux density
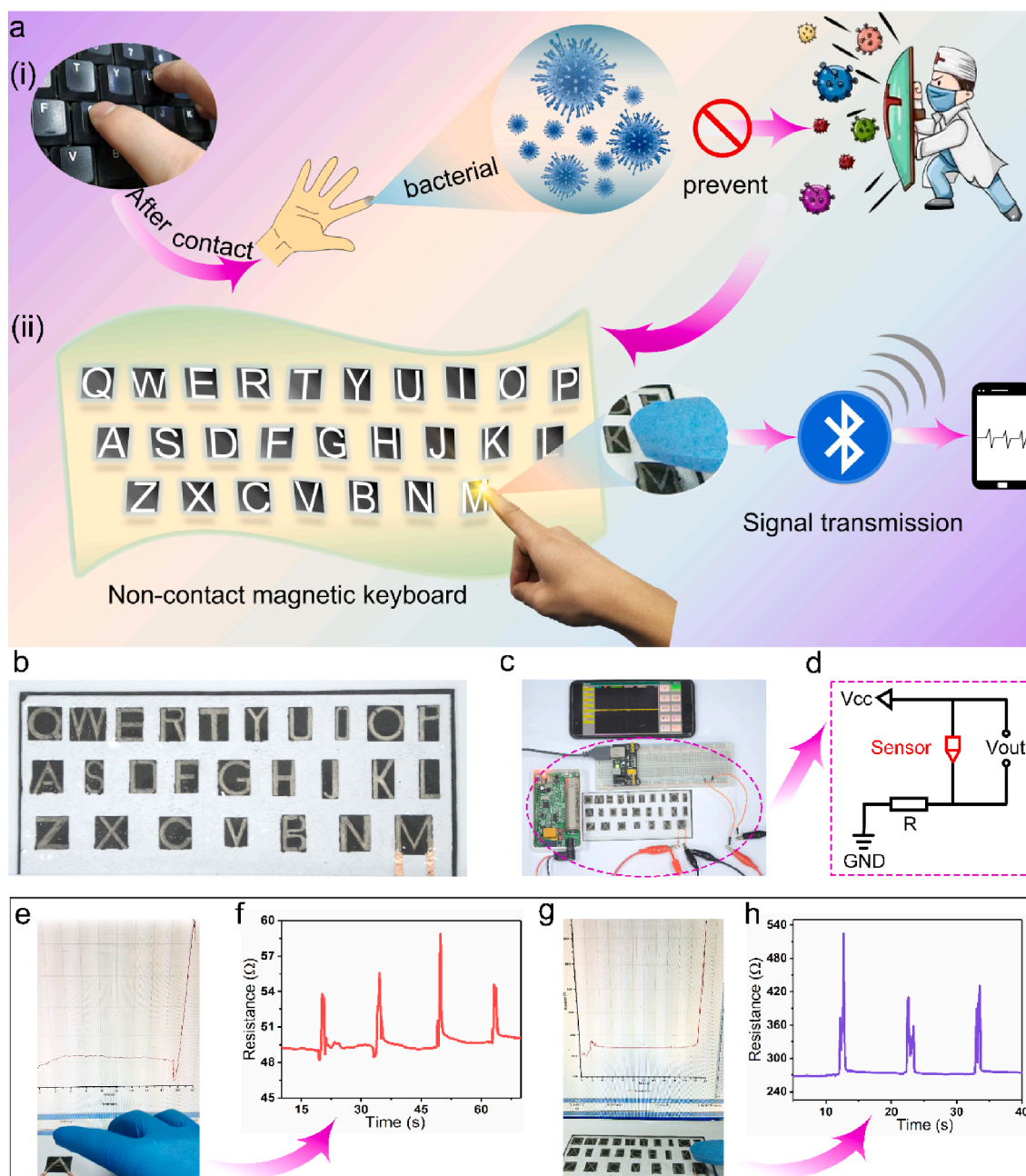
Fig. 9. Non-contact sensing performance. (a) Schematic of SSF for non-contact magnetic keyboard, (i) Potential application of a keyboard in daily life, (ii) Schematic diagram and signal acquisition of the non-contact magnetic keyboard; The optical image of (b) non-contact magnetic keyboard; The images of (c) wireless keyboard sensing system based on the SSF sensor; (d) Circuit of this wireless sensing system; (e, g) The Modulab MTS test images and (f, h) the electrical response of single alphabet and non-contact magnetic keyboard, respectively.

increased from 45 mT to 205 mT, the $\Delta R/R_0$ of SSF sensor under the attractive force varied from 2.1% to 9.9%. Furthermore, based on the magnetic SSF sensor, a non-contact magnetic keyboard was designed and fabricated. Therefore, due to these outstanding properties and functions, SSF sensor is promising to be employed as wearable electronic skin and non-contact keyboard systems.

Declaration of Competing Interest

The authors declare that they have no known competing financial interests or personal relationships that could have appeared to influence the work reported in this paper.

Appendix A. Supplementary data

Supplementary data to this article can be found online at https://doi.org/10.1016/j.cej.2021.134424.

References

[1] Y.X. Zhuang, R.J. Xie, Mechanoluminescence rebrightening the prospects of stress sensing: a review, Adv. Mater. (2021) 2005925, https://doi.org/10.1002/adma.202005925.

[2] L.J. Lu, C.P. Jiang, G.S. Hu, J.Q. Liu, B. Yang, Flexible noncontact sensing for human-machine interaction, Adv. Mater. 33 (2021) 2100218, https://doi.org/10.1002/adma.202100218.

[3] J.P. Wu, H.M. Pang, L. Ding, Y. Wang, X.K. He, Q. Shu, S.H. Xuan, X.L. Gong, A lightweight, ultrathin aramid-based flexible sensor using a combined inkjet printing and buckling strategy, Chem. Eng. J. 421 (2021), 129830, https://doi.org/10.1016/j.cej.2021.129830.

[4] S. Pyo, J. Lee, K. Bae, S. Sim, J. Kim, Recent progress in flexible tactile sensors for human-interactive systems: from sensors to advanced applications, Adv. Mater. (2021) 2005902, https://doi.org/10.1002/adma.202005902.

[5] T.G. Thuruthel, B. Shih, C. Laschi, M.T. Tolley, Soft robot perception using embedded soft sensors and recurrent neural networks, Sci. Robot. 4 (2019) 1488, https://doi.org/10.1126/scirobotics.aav1488.

[6] M.L. Zhu, Z.D. Sun, Z.X. Zhang, Q.F. Shi, T.Y.Y. He, H.C. Liu, T. Chen, C.K. Lee, Haptic-feedback smart glove as a creative human-machine interface (HMI) for virtual/augmented reality applications, Sci. Adv. 6 (2020) 8693, https://doi.org/10.1126/sciadv.aaz8693.

[7] H.C. Wang, R.C. Zhou, D.H. Li, L.R. Zhang, G.Z. Ren, L. Wang, J.H. Liu, D.Y. Wang, Z.H. Tang, G. Lu, G.Z. Sun, H.D. Yu, W. Huang, High-performance foam-shaped strain sensor based on carbon nanotubes and Ti$_3$C$_2$T$_x$ MXene for the monitoring of human activities, ACS Nano 15 (2021) 9690–9700, https://doi.org/10.1021/acsnano.1c00259.

[8] G. Muscas, P.E. Jönsson, I.G. Serrano, Ö. Vallin, M.V. Kamalakar, Ultralow magnetostrictive flexible ferromagnetic nanowires, Nanoscale 13 (12) (2021) 6043–6052, https://doi.org/10.1039/D0NR08355K.

[9] L.i. Ding, Y.u. Wang, C. Sun, Q. Shu, T. Hu, S. Xuan, X. Gong, Three-dimensional structured dual-mode flexible sensors for highly sensitive tactile perception and noncontact sensing, ACS Appl. Mater. Inter. 12 (18) (2020) 20955–20964, https://doi.org/10.1021/acsami.0c03996.

[10] S. Ota, A. Ando, D. Chiba, A flexible giant magnetoresistive device for sensing strain direction, Nat. Electron. 1 (2) (2018) 124–129, https://doi.org/10.1038/s41928-018-0022-3.

[11] H. Jia, X. Yang, Q.Q. Kong, L.J. Xie, Q.G. Guo, G.e. Song, L.L. Liang, J.P. Chen, Y. Li, C.M. Chen, Free-standing, anti-corrosion, super flexible graphene oxide/silver nanowire thin films for ultra-wideband electromagnetic interference shielding, J. Mater. Chem. A 9 (2) (2021) 1180–1191, https://doi.org/10.1039/D0TA09246K.

[12] M. Ha, G.S. Cañón Bermúdez, J.A.C. Liu, E.S. Oliveros Mata, B.A. Evans, J.B. Tracy, D. Makarov, Reconfigurable magnetic origami actuators with on-board sensing for guided assembly, Adv. Mater. 33 (2021) 2008751, https://doi.org/10.1002/adma.202008751.

[13] P. Makushko, E.S. Oliveros Mata, G.S. Cañón Bermúdez, M. Hassan, S. Laureti, C. Rinaldi, F. Fagiani, G. Barucca, N. Schmidt, Y. Zabila, T. Kosub, R. Illing, O. Volkov, I. Vladymyrskyi, J. Fassbender, M. Albrecht, G. Varvaro, D. Makarov, Flexible magnetoreceptor with tunable intrinsic logic for on-skin touchless human-machine interfaces, Adv. Funct. Mater. 31 (2021), https://doi.org/10.1002/adfm.202101089.

[14] Q. Zhou, B. Ji, B. Hu, S. Li, Y. Xu, Y. Gao, W. Wen, J. Zhou, B. Zhou, Tilted magnetic micropillars enabled dual-mode sensor for tactile/touchless perceptions, Nano Energy 78 (2020), 105382, https://doi.org/10.1016/j.nanoen.2020.105382.

[15] S. Bhatti, C. Ma, X. Liu, S.N. Piramanayagam, Stress-induced domain wall motion in FeCo-based magnetic microwires for realization of energy harvesting, Adv. Electron. Mater. 5 (2019) 1800467, https://doi.org/10.1002/aelm.201800467.

[16] Z. Wu, H. Ding, K. Tao, Y. Wei, X. Gui, W. Shi, X.i. Xie, J. Wu, Ultrasensitive, stretchable, and fast-response temperature sensors based on hydrogel films for wearable applications, ACS Appl. Mater. Inter. 13 (18) (2021) 21854–21864, https://doi.org/10.1021/acsami.1c05291.

[17] S.X. Bao, J.T. Gao, T.F. Xu, N. Li, W.X. Chen, W.Y. Lu, Anti-freezing and antibacterial conductive organohydrogel co-reinforced by 1D silk nanofibers and 2D graphitic carbon nitride nanosheets as flexible sensor, Chem. Eng. J. 411 (2021), 128470, https://doi.org/10.1016/j.cej.2021.128470.

[18] D.Z. Chen, T.S. Chen, Y. Li, S.X. Li, L. Zhang, Y.W. Ren, Y.W. Wang, J.H. Liang, T. Fu, M. Zhang, X.H. He, A flexible sensor based on 3D gold@carbonaceous nanohybrid with defect sites of conductivity for the wearable sensing at low stress, Nano 16 (2021) 2150044, https://doi.org/10.1142/S1793292021500442.

[19] Z. Yang, Z. Wu, Z. Diang, R. Wei, X. Mai, D. Pan, S. Vupputuri, L. Weng, N. Naik, Z. Guo, Ultra-sensitive flexible sandwich structural strain sensors based on a silver nanowire supported PDMS/PVDF electrospun membrane substrate, J. Mater. Chem. C 9 (8) (2021) 2752–2762, https://doi.org/10.1039/D0TC04659K.

[20] Z. Wu, C. Cao, Q. Sun, F. Zhong, M. Zhang, H. Duan, Mechanical, thermal and gas sensing properties of flexible multi-walled carbon nanotubes/waterborne polyurethane composite film, Compos. Sci. Technol. 216 (2021), 109040, https://doi.org/10.1016/j.compscitech.2021.109040.

[21] L.i. Ding, S. Xuan, L. Pei, S. Wang, T. Hu, S. Zhang, X. Gong, Stress and magnetic field bimode detection sensors based on flexible CI/CNTs-PDMS sponges, ACS Appl. Mater. Inter. 10 (36) (2018) 30774–30784, https://doi.org/10.1021/acsami.8b11333.

[22] S. Wang, Z. Sun, Y. Zhao, L. Zuo, A highly stretchable hydrogel sensor for soft robot multi-modal perception, Sens. Actuators A, Phys.cal 331 (2021), 113006, https://doi.org/10.1016/j.sna.2021.113006.

[23] T. Hu, S. Xuan, L. Ding, X. Gong, Liquid metal circuit based magnetoresistive strain sensor with discriminating magnetic and mechanical sensitivity, Sens. Actuators, B 314 (2020), 128095, https://doi.org/10.1016/j.snb.2020.128095.

[24] S. Wang, J. Xu, W. Wang, G.J. Wang, R. Rastak, F. Molina-Lopez, J.W. Chung, S. Niu, V.R. Feig, J. Lopez, T. Lei, S.K. Kwon, Y. Kim, A.M. Foudeh, A. Ehrlich, A. Gasperini, Y. Yun, B. Murmann, J.-H. Tok, Z. Bao, Skin electronics from scalable fabrication of an intrinsically stretchable transistor array, Nature 555 (7694) (2018) 83–88, https://doi.org/10.1038/nature25494.

[25] S. Sundaram, P. Kellnhofer, Y. Li, J.Y. Zhu, A. Torralba, W. Matusik, Learning the signatures of the human grasp using a scalable tactile glove, Nature 569 (7758) (2019) 698–702, https://doi.org/10.1038/s41586-019-1234-z.

[26] H.S. Wang, S.K. Hong, J.H. Han, Y.H. Jung, H.K. Jeong, T.H. Im, C.K. Jeong, B. Y. Lee, G. Kim, C.D. Yoo, K.J. Lee, Biomimetic and flexible piezoelectric mobile acoustic sensors with multiresonant ultrathin structures for machine learning biometrics, Sci. Adv. 7 (2021) 5683, https://doi.org/10.1126/sciadv.abe5683.

[27] R. Shi, Z. Lou, S. Chen, G. Shen, Flexible and transparent capacitive pressure sensor with patterned microstructured composite rubber dielectric for wearable touch keyboard application, Sci. China Mater.. 61 (12) (2018) 1587–1595, https://doi.org/10.1007/s40843-018-9267-3.

[28] X. Liu, X. Liang, Z. Lin, Z. Lei, Y. Xiong, Y. Hu, P. Zhu, R. Sun, C.P. Wong, Highly sensitive and stretchable strain sensor based on a synergistic hybrid conductive network, ACS Appl. Mater. Inter. 12 (37) (2020) 42420–42429, https://doi.org/10.1021/acsami.0c12642.

[29] J.H. Yang, R.L. Shi, Z. Lou, R.Q. Chai, K. Jiang, G.Z. Shen, Flexible smart noncontact control systems with ultrasensitive humidity sensors, Small 15 (2019) 1902801, https://doi.org/10.1002/smll.201902801.

[30] X.Y. Meng, J.H. Yang, Z.G. Liu, W.B. Lu, Y.M. Sun, Y.Q. Dai, Compos. Commun. 20 (2020), 100347, https://doi.org/10.1016/j.coco.2020.04.013.

[31] W.R. Johnson, A. Mian, M.A. Robinson, J. Verheul, D.G. Lloyd, J.A. Alderson, Multidimensional ground reaction forces and moments from wearable sensor accelerations *via* deep learning, IEEE T. Biomed. Eng. 68 (1) (2021) 289–297, https://doi.org/10.1109/TBME.2020.3006158.

[32] S.S. Thakur, S.S. Abdul, H.S. Chiu, R.B. Roy, P.Y. Huang, S. Malwade, A. A. Nursetyo, Y.J. Li, Artificial-intelligence-based prediction of clinical events among hemodialysis patients using non-contact sensor data, Sensors 18 (2018) 2833, https://doi.org/10.3390/s18092833.

[33] J. Wu, Y.M. Sun, Z. Wu, X. Li, N. Wang, K. Tao, G.P. Wang, Carbon nanocoil-based fast-response and flexible humidity sensor for multifunctional applications, ACS Appl. Mater. Inter. 11 (4) (2019) 4242–4251, https://doi.org/10.1021/acsami.8b18599.

[34] C. Yang, H.W. Gu, W. Lin, M.M. Yuen, C.P. Wong, M.Y. Xiong, B. Gao, Silver nanowires: from scalable synthesis to recyclable foldable electronics, Adv. Mater. 23 (2011) 3052–3056, https://doi.org/10.1002/adma.201100530.